INTERNATIONAL JOURNAL FOR NUMERICAL METHODS IN FLUIDS
Int. J. Numer. Meth. Fluids 2008; **58**:659–685

Implementation of high-order compact finite-difference method to parabolized Navier–Stokes schemes

Vahid Esfahanian[1,‡], Kazem Hejranfar[2,*,†,§] and Hossein Mahmoodi Darian[1,¶]

[1]*Mechanical Engineering Department, University of Tehran, Tehran, Iran*
[2]*Aerospace Engineering Department, Sharif University of Technology, Tehran, Iran*

SUMMARY

The numerical solution to the parabolized Navier–Stokes (PNS) and globally iterated PNS (IPNS) equations for accurate computation of hypersonic axisymmetric flowfields is obtained by using the fourth-order compact finite-difference method. The PNS and IPNS equations in the general curvilinear coordinates are solved by using the implicit finite-difference algorithm of Beam and Warming type with a high-order compact accuracy. A shock-fitting procedure is utilized in both compact PNS and IPNS schemes to obtain accurate solutions in the vicinity of the shock. The main advantage of the present formulation is that the basic flow variables and their first and second derivatives are simultaneously computed with the fourth-order accuracy. The computations are carried out for a benchmark case: hypersonic axisymmetric flow over a blunt cone at Mach 8. A sensitivity study is performed for the basic flowfield, including profiles and their derivatives obtained from the fourth-order compact PNS and IPNS solutions, and the effects of grid size and numerical dissipation term used are discussed. The present results for the flowfield variables and also their derivatives are compared with those of other basic flow models to demonstrate the accuracy and efficiency of the proposed method. The present work represents the first known application of a high-order compact finite-difference method to the PNS schemes, which are computationally more efficient than Navier–Stokes solutions. Copyright © 2008 John Wiley & Sons, Ltd.

Received 10 April 2006; Revised 11 October 2007; Accepted 2 January 2008

KEY WORDS: hypersonic axisymmetric flows; compact finite-difference method; PNS equations; iterated PNS (IPNS) equations

---

[*] Correspondence to: Kazem Hejranfar, Aerospace Engineering Department, Sharif University of Technology, Tehran, Iran.

[†] E-mail: khejran@sharif.edu

[‡] Professor.

[§] Assistant Professor.

[¶] Ph.D. Candidate.

Contract/grant sponsor: University of Tehran
Contract/grant sponsor: Sharif University of Technology

1. INTRODUCTION

Owing to high sensitivity of some problems, such as flow stability analysis to accuracy of basic flow variables, using high accuracy numerical methods for solving basic flow variables is essential. Traditional high accuracy finite-difference methods use larger stencil sizes that make boundary treatment difficult. Moreover, spectral methods are restricted to special grids, whereas compact methods are capable of producing higher order accuracies without any increase in numerical stencil. Compared with the traditional finite-difference schemes of the same order of accuracy, compact schemes have been proved to be significantly more accurate with the added benefit of using smaller stencil sizes, which can be essential when treating nonperiodic boundary conditions [1, 2].

The objective of the present work is to implement a fourth-order compact finite-difference method to the parabolized Navier–Stokes (PNS) equations for accurate computation of hypersonic flows. The study has been shown that the PNS schemes can be used for an efficient and fast computing the basic flow and the associated flow stability results in hypersonic speeds [3, 4]. It was also found that the stability results are more sensitive to the accuracy of the basic flowfield and the derivatives of the flow variables [3–5]. Therefore, by implementation of the high-order compact finite-difference method to the PNS schemes [6–8], accurate basic flow models suitable for the stability analysis and transition prediction of hypersonic flows are efficiently provided.

In the present work, the high-order accurate solution to hypersonic axisymmetric flows is obtained by implementing a fourth-order compact finite-difference method based on an implicit algorithm to both PNS and globally iterated PNS (IPNS) equations. A shock-fitting procedure is used in both PNS and IPNS compact schemes to obtain accurate solutions in the vicinity of the shock. The main advantage of the present formulation is that the basic flow profiles and their first and second derivatives, required for the flow stability analysis, are automatically computed with the fourth-order accuracy. At first, the dispersive and dissipative properties of the compact methods are discussed. Then, the fourth-order compact method is implemented to the quasi-one-dimensional Euler equations to solve compressible flow inside the Shubin nozzle. Finally, the results of the fourth-order compact finite-difference method for the PNS and IPNS schemes are presented for hypersonic axisymmetric flow over a blunt cone at Mach 8. The present computations for the basic flow variables and also their derivatives are compared with those of other basic flow models to demonstrate the accuracy and efficiency of the proposed method. A sensitivity study is also performed for the basic flow variables and their derivatives obtained from the fourth-order compact PNS schemes, and the effects of grid size and numerical dissipation term used are investigated.

2. GOVERNING EQUATIONS

2.1. The PNS equations

The thin layer Navier–Stokes (TLNS) equations are obtained from the full Navier–Stokes equations by neglecting viscous terms associated with the streamwise derivatives. The PNS equations are obtained by dropping the unsteady term in the TLNS equations and modifying the streamwise pressure gradient in the streamwise momentum equation to permit stable marching. The PNS equations for axisymmetric compressible flow can be expressed in dimensionless and conservation forms in the generalized coordinate system (ξ, η) as follows:

$$\begin{gathered}\frac{\partial \bar{F}}{\partial \xi}+\frac{\partial \bar{G}}{\partial \eta}+\bar{H}=0 \\ \bar{F}=\bar{F}_{\mathrm{i}}, \quad \bar{G}=\bar{G}_{\mathrm{i}}-\bar{G}_{\mathrm{v}}, \quad \bar{H}=\bar{H}_{\mathrm{i}}-\bar{H}_{\mathrm{v}}\end{gathered} \tag{1}$$

where the solution vector is

$$\bar{U}=J^{-1}\widetilde{U}=J^{-1}[\rho, \rho u, \rho v, E]^{\mathrm{T}}$$

$\bar{F}_{\mathrm{i}}$, $\bar{G}_{\mathrm{i}}$ and $\bar{H}_{\mathrm{i}}$ are the inviscid flux vectors and $\bar{G}_{\mathrm{v}}$ and $\bar{H}_{\mathrm{v}}$ are the viscous flux vectors.

The PNS equations are a mixed set of hyperbolic–parabolic equations in the marching direction, provided the inviscid flow is supersonic, the streamwise velocity component is everywhere positive, and either the streamwise pressure gradient term is dropped in the subsonic region or the departure behavior is suppressed using a suitable technique. The presence of the streamwise pressure gradient term in the streamwise convective flux vector permits the upstream influences to occur in the subsonic region of the boundary layer, which leads to exponentially growing solutions referred to as departure solutions [9]. Stable marching of numerical solution to the PNS equations is achieved in the subsonic region of the boundary layer by using the methods proposed by Vigneron *et al.* [10] and Schiff and Steger [11]. For this study, the Vigneron *et al.* [10] technique is implemented to prevent departure solutions.

In the Vigneron *et al.* approximation, the streamwise pressure gradient in the momentum equations is split into an implicit contribution and an explicit contribution:

$$\frac{\partial p}{\partial \xi}=\left[\omega \frac{\partial p}{\partial \xi}\right]_{\text{implicit}}+\left[(1-\omega) \frac{\partial p}{\partial \xi}\right]_{\text{explicit}} \tag{2}$$

The weighting function ω is determined as

$$\omega=\min \left[1, \frac{\sigma \gamma M_{\xi}^{2}}{1+(\gamma-1) M_{\xi}^{2}}\right] \tag{3}$$

where M_{ξ} is the local streamwise Mach number and σ is a safety factor to account for nonlinearities in the analysis. The value of σ in the pressure correction relation should be very close to 1; otherwise undesirable oscillations appear around the sonic line, especially in the pressure profile. To introduce the Vigneron *et al.* technique into the PNS equations, a new vector $\bar{F}^{*}$ is defined as

$$\bar{F}^{*}=\bar{F}-P \tag{4}$$

Thus, the new form of the PNS equations appears as

$$\frac{\partial \bar{F}^{*}}{\partial \xi}+\frac{\partial P}{\partial \xi}+\frac{\partial \bar{G}}{\partial \eta}+\bar{H}=0 \tag{5}$$

where the inviscid vectors F^* and P are

$$\bar{F}^* = J^{-1}\begin{pmatrix} \rho U_{\mathrm{c}} \\ \rho u U_{\mathrm{c}} + \omega \xi_x p \\ \rho v U_{\mathrm{c}} + \omega \xi_y p \\ (E+p) U_{\mathrm{c}} \end{pmatrix}, \quad P = J^{-1}\begin{pmatrix} 0 \\ (1-\omega)\xi_x p \\ (1-\omega)\xi_y p \\ 0 \end{pmatrix}$$

where (u, v) are the Cartesian velocity components, U_{c} denotes the contravariant velocity in the ξ direction $U_{\mathrm{c}} = \xi_x u + \xi_y v$, ρ is the density, p is the pressure and E is the total energy per unit volume. In this study, the ratio of specific heats is assumed to be constant, $\gamma = 1.4$, the molecular viscosity μ is determined by the Sutherland law and the coefficient of thermal conductivity is calculated by assuming a constant Prandtl number, $Pr = 0.72$. Finally, the system of PNS equations is closed by employing the perfect-gas equations of state. The preceding equations have been nondimensionalized using the reference length L (R_{N} dimensional nose radius) and free-stream conditions.

In the present PNS solver, the 'elliptic' part of the streamwise pressure gradient term ($\partial P/\partial \xi$) responsible for upstream disturbance propagation is omitted to permit the space-marching procedure to be stable. This term will be treated explicitly in the IPNS equations as discussed in the following subsection.

2.2. *The IPNS equations*

For solving the flowfields with significant upstream influences, omission of the explicit part of the streamwise pressure gradient may affect the accuracy of basic flow variables and their derivatives. In these cases, the globally IPNS equations, called the reduced Navier–Stokes (RNS) equations, can be used and the upstream influences are taken into account by the forward differencing of the elliptic part of streamwise pressure gradient. The globally IPNS scheme has been used by several investigators. The IPNS model presented herein is based on the method proposed by Barnett and Davis [12]. This IPNS scheme utilizes an alternating direction explicit (ADE) procedure, which is in the form of a two-step calculation procedure for each global iteration. In the ADE method, the streamwise pressure gradient is split using Vigneron's technique and a fictitious unsteady term is appended to the elliptic part as follows:

$$\frac{\partial p}{\partial \xi} = \omega \frac{\partial p}{\partial \xi} + (1-\omega)\left[\frac{\partial p}{\partial \xi} - \frac{\partial p}{\partial t}\right] \tag{6}$$

to permit the upstream propagation of information through the subsonic region in a hyperbolic manner. Because the IPNS scheme employs the full pressure gradient term in the subsonic region of the boundary layer, it can give a solution comparable with that of the TLNS scheme [3, 4]. Thus, by implementing the fourth-order compact finite-difference method to the IPNS scheme, a high-order accurate basic flow model appropriate for the stability analysis of hypersonic flows can be efficiently provided.

2.3. *Boundary conditions and initial data*

The boundary conditions at the wall consist of no-slip conditions for the velocity components, a specified wall-temperature or an adiabatic wall, and zero pressure gradient approximation normal

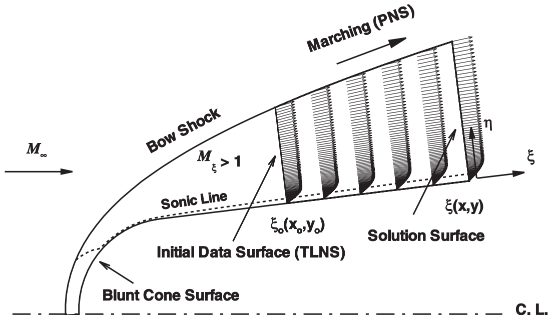

Figure 1. Marching procedure and initial data surface for starting the PNS solution over a blunt cone. The figure also shows the development of the velocity field.

to the wall. The wall for the cases studied here is assumed to be adiabatic. At the upper boundary, the bow shock is fitted using a shock-fitting technique to obtain an accurate solution to the PNS equations near the shock. The advantage of the shock-fitting method over the shock-capturing method is its capability to produce oscillation-free profiles, especially in the vicinity of the strong shocks thus improving the accuracy of the results.

The PNS equations are not self-starting for blunt body computations and therefore need appropriate initial conditions. The starting data of the PNS equations are provided by the solution to the TLNS equations [5, 13] for the blunt cone. The TLNS equations in the nose region are solved by the second-order method with fine grid in order to have the initial data with sufficient accuracy. Figure 1 shows the initial conditions and the marching procedure for the solution to the PNS equations. The starting solution on an initial data surface where the inviscid flow is supersonic is obtained from the solution to the TLNS model [5, 13].

2.4. Computational grid

An algebraic grid scheme is used to compute flowfield. The lines of constant ξ are distributed uniformly along the body surface and are orthogonal to the body. To ensure that the viscous regions are adequately resolved, the lines of constant η are clustered near the body surface according to [9]

$$\frac{x-x_w}{x_s-x_w}=\bar{a}, \quad \frac{y-y_w}{y_s-y_w}=\bar{a} \tag{7}$$

where

$$\bar{a}=1+\bar{\beta}\left[\frac{1-\tilde{a}^{(1-\eta/\eta_{\max})}}{1+\tilde{a}^{(1-\eta/\eta_{\max})}}\right], \quad \tilde{a}=\frac{\bar{\beta}+1}{\bar{\beta}-1}$$

in which the clustering parameter $\bar{\beta}$ is assigned to be 1.01 for all calculations. The above grid is used for both PNS and IPNS equations.

3. NUMERICAL SIMULATION

The numerical solutions to the PNS and IPNS equations in the generalized coordinate system are obtained by using an implicit finite-difference methods in the wall-normal direction η similar to the Beam and Warming method [3, 4, 14], in which the basic flow variables and their first and second derivatives are automatically computed with the fourth-order accuracy [6–8]. The numerical algorithm of the PNS equations for a marching step $\Delta\xi$ using the first-order backward Euler implicit scheme can be expressed in delta form as

$$\Delta\bar{F}^{*i}+\Delta\xi\left[\frac{\partial\Delta\bar{G}}{\partial\eta}+\Delta\bar{H}\right]^i=-\Delta\xi\left[\frac{\partial\bar{G}}{\partial\eta}+\bar{H}\right]^i-\Delta P^i \tag{8}$$

After linearization, the equations are reduced to the following nonconservative form:

$$C_0\Delta\bar{U}^i+C_1\Delta\bar{U}^i_\eta+C_2\Delta\bar{U}^i_{\eta\eta}=C_R \tag{9}$$

where $\Delta\bar{U}^i=\bar{U}^{i+1}-\bar{U}^i$ and $()_\eta=\mathrm{d}/\mathrm{d}\eta$ represents the derivative with respect to η. When the traditional central scheme is used, the unknowns are $\Delta\bar{U}^i$, the blocks are 4×4 and the matrix of coefficients is tridiagonal. Using a traditional fourth-order differencing does not keep this matrix tridiagonal, whereas the present compact formulation keeps the tridiagonality of the system of equations at the expense of having 12×12 blocks. The following fourth-order compact relations for the first and second derivatives are used $(f'=\Delta\bar{U}_\eta,\ f''=\Delta\bar{U}_{\eta\eta})$:

$$\begin{aligned}\frac{f'_{j+1}+4f'_j+f'_{j-1}}{6}&=\frac{f_{j+1}-f_{j-1}}{2\Delta\eta}+O(\Delta\eta)^4\\ \frac{f''_{j+1}+10f''_j+f''_{j-1}}{12}&=\frac{f_{j+1}-2f_j+f_{j-1}}{(\Delta\eta)^2}+O(\Delta\eta)^4\end{aligned} \tag{10}$$

to complete the system of equations for computing the flowfield. In addition to having less truncation error of the present formulation of the compact method in comparison with the traditional fourth-order scheme, the main advantage of the present formulation is that the basic flow variables and their first and second derivatives, required for the flow stability analysis, are simultaneously computed with the fourth-order accuracy. It has been shown that the traditional finite-difference method for the discrete differentiation of the basic flow profiles causes oscillations near the wall where high clustering grid points are used [3, 4]. The present formulation causes less numerical oscillations compared with the traditional method.

3.1. Numerical dissipation term

High-order dissipation term must be added to damp high-frequency oscillations associated with the central differencing of derivatives in the η-direction. Herein, a sixth-order dissipation term is used to stabilize the numerical instability of the method

$$D_e=\varepsilon_e\left[\frac{\partial\bar{F}^*}{\partial\bar{U}}\right]^i(\nabla_\eta\Delta_\eta)^3\bar{U}^i \tag{11}$$

DOI: 10.1002/fld

This term is added to the right-hand side of Equation (9). The stability bound for the dissipation coefficient is obtained from the stability analysis of the numerical method, $0 \leqslant \varepsilon_e \leqslant 1/32$ (see Appendix A).

The present study demonstrates that the basic flow profiles and their derivatives based on high-order compact methods are sensitive to the grid size, especially the numerical dissipation term used in computing the flowfield, as discussed in the Numerical Results section.

3.2. Boundary treatment

The no-slip conditions for the velocity components on the wall using the conservative variables are

$$\bar{U}_2^{i+1} = \bar{U}_3^{i+1} = 0 \quad \text{implies} \quad \Delta\bar{U}_2^i = \Delta\bar{U}_3^i = 0 \tag{12}$$

where subscripts indicate the elements of $\Delta\bar{U}^i$ and not the grid numbers. Also the zero pressure gradient approximation normal to the wall along with the no-slip conditions gives

$$\left.\frac{\partial p}{\partial \eta}\right|_{\text{wall}} = 0 \quad \text{implies} \quad \frac{\partial}{\partial \eta}(J\bar{U}_4)^{i+1} = 0 \tag{13}$$

or

$$J_\eta^{i+1}\Delta\bar{U}_4^i + J^{i+1}(\Delta\bar{U}_4^i)_\eta = -(J_\eta^{i+1}\bar{U}_4^i + J^{i+1}(\bar{U}_4^{i+1})_\eta) \tag{14}$$

and the adiabatic wall with the above zero pressure gradient yields

$$\left.\frac{\partial \rho}{\partial \eta}\right|_{\text{wall}} = 0 \quad \text{implies} \quad J_\eta^{i+1}\Delta\bar{U}_1^i + J^{i+1}(\Delta\bar{U}_1^i)_\eta = -(J_\eta^{i+1}\bar{U}_1^i + J^{i+1}(\bar{U}_1^{i+1})_\eta) \tag{15}$$

Note that Equations (14) and (15) are in the form of Equation (9). Finally, at the shock boundary, the flow variables are initially assumed to be the same as the previous marching step (conical flow assumption), that is,

$$(J\bar{U})^{i+1} = (J\bar{U})^i \quad \text{implies} \quad J^{i+1}\Delta\bar{U}^i = (J^i - J^{i+1})\bar{U}^i \tag{16}$$

At each station, the shock slope and the flow variables are iteratively corrected by using compatibility and Rankine–Hugoniot relations in an explicit manner. The iterative process is repeated at the shock until the solution converges, and then the solution marches on the next solution plane.

To have a tridiagonal system of equations, two two-point compact third-order schemes are used for the points adjacent to the wall and shock boundaries

$$\begin{aligned} f_j - f_{j+1} + (\Delta\eta) f_j' + \frac{(\Delta\eta)^2}{6}(2f_j'' + f_{j+1}'') + O(\Delta\eta)^4 = 0 \\ f_j - f_{j+1} + (\Delta\eta) f_{j+1}' - \frac{(\Delta\eta)^2}{6}(f_j'' + 2f_{j+1}'') + O(\Delta\eta)^4 = 0 \end{aligned} \tag{17}$$

The simplicity of treating boundary conditions of Von Neumann type with the compact method is one of the advantages of using compact schemes and is worth mentioning here. The boundary finite difference schemes (17) allow applying boundary conditions, Equations (14) and (15), without missing the tridiagonality of the system of equations while preserving the third-order accuracy at the boundaries.

3.3. Block tridiagonal system of equations

The preceding system of Equations (9) and (10) along with the above boundary conditions forms a block tridiagonal system of equations for $\{X\}=\{\Delta\bar{U}^i, \Delta\bar{U}^i_\eta, \Delta\bar{U}^i_{\eta\eta}\}^{\mathrm{T}}$ with a block size of 12×12 as follows:

$$[M]\{X\}=\{R\}$$

$$[M]=\begin{bmatrix} B_1 & D_1 & & & \\ \ddots & \ddots & \ddots & & \\ & A_j & B_j & D_j & \\ & & \ddots & \ddots & \ddots \\ & & & A_{J_{\max}} & B_{J_{\max}} \end{bmatrix}, \quad \{X\}=\begin{Bmatrix} X_1 \\ \vdots \\ X_j \\ \vdots \\ X_{J_{\max}} \end{Bmatrix}, \quad \{R\}=\begin{Bmatrix} R_1 \\ \vdots \\ R_j \\ \vdots \\ R_{J_{\max}} \end{Bmatrix} \tag{18}$$

where the block elements and unknown and right-hand side vectors are

$$B_1=\begin{bmatrix} C_0 & C_1 & C_2 \\ I & hI & \dfrac{h^2}{3}I \\ I & O & -\dfrac{h^2}{6}I \end{bmatrix}, \quad D_1=\begin{bmatrix} O & O & O \\ -I & O & \dfrac{h^2}{6}I \\ -I & hI & -\dfrac{h^2}{3}I \end{bmatrix}$$

$$A_j=\begin{bmatrix} O & O & O \\ -I & -\dfrac{h}{3}I & O \\ I & O & -\dfrac{h^2}{12}I \end{bmatrix}, \quad B_j=\begin{bmatrix} C_0 & C_1 & C_2 \\ O & -\dfrac{4h}{3}I & O \\ -2I & O & -\dfrac{10h^2}{12}I \end{bmatrix}$$

$$D_j=\begin{bmatrix} O & O & O \\ I & -\dfrac{h}{3}I & O \\ I & O & -\dfrac{h^2}{12}I \end{bmatrix}, \quad 2\leqslant j\leqslant J_{\max}-1$$

$$A_{J_{\max}}=\begin{bmatrix} O & O & O \\ -I & -hI & -\dfrac{h^2}{3}I \\ -I & O & \dfrac{h^2}{6}I \end{bmatrix}, \quad B_{J_{\max}}=\begin{bmatrix} C_0 & C_1 & C_2 \\ I & O & -\dfrac{h^2}{6}I \\ I & -hI & \dfrac{h^2}{3}I \end{bmatrix}$$

$$X_j = \left\{ \begin{matrix} \Delta U \\ \Delta U_\eta \\ \Delta U_{\eta\eta} \end{matrix} \right\}, \quad R_j = \left\{ \begin{matrix} C_R \\ O \\ O \end{matrix} \right\}$$

where I is a 4×4 identity matrix and O is a 4×4 zero matrix or zero vector of length 4. Matrices C_0, C_1 and C_2 introduce the governing equations (1) and also the boundary conditions into the system of equations.

A block-tridiagonal solver is used to calculate the incremental solution vector $\{X\} = \{\Delta\bar{U}^i, \Delta\bar{U}^i_\eta, \Delta\bar{U}^i_{\eta\eta}\}^{\mathrm{T}}$, and then the flow variables and the first and second derivatives are automatically determined as follows:

$$\begin{aligned} \bar{U}^{i+1} &= \bar{U}^i + \Delta\bar{U}^i \\ \bar{U}^{i+1}_\eta &= \bar{U}^i_\eta + \Delta\bar{U}^i_\eta \\ \bar{U}^{i+1}_{\eta\eta} &= \bar{U}^i_{\eta\eta} + \Delta\bar{U}^i_{\eta\eta} \end{aligned} \tag{19}$$

3.4. Solution to IPNS equations

As mentioned before, for computing the flowfield using the single sweep PNS scheme, the explicit streamwise pressure gradient term ΔP^i in Equation (8) is dropped. For the solution to the IPNS model, the above algorithm can be used and the streamwise pressure gradient term is treated by employing the ADE procedure. The ADE method, using a first-order forward difference formula for the explicit pressure gradient term in Equation (6), is expressed in two steps as follows:

First step:

$$\left.\frac{\partial p}{\partial \xi}\right|^{i+1} = \omega \frac{p_m^{i+1} - p_m^i}{\Delta\xi} + (1-\omega)\left[\frac{p_k^{i+1} - p_k^i}{\Delta\xi} - \frac{p_m^{i+1} - p_k^{i+1}}{\Delta t}\right] \tag{20}$$

In this step, the PNS equations are solved with the streamwise pressure gradient given by Equation (20). The solution is marched from the upstream to the downstream boundary to obtain the pressure distribution at the intermediate time level p_m.

Second step:

$$\frac{p_k^{i+2} - p_k^{i+1}}{\Delta\xi} - \frac{p_m^{i+1} - p_k^{i+1}}{\Delta t} = \frac{p_{k+1}^{i+2} - p_{k+1}^{i+1}}{\Delta\xi} - \frac{p_{k+1}^{i+1} - p_m^{i+1}}{\Delta t} \tag{21}$$

The above equation is solved by marching the solution from the downstream to the upstream boundary to obtain the pressure at the new time level p_{k+1}. This simple relation enforces the propagation of information upstream in a relatively rapid manner.

An appropriate outflow boundary condition for the IPNS solution is provided by setting the streamwise pressure gradient equal to zero at the outer boundary. The IPNS solution requires the initial pressure distribution in the subsonic region. The initial guess can be adequately provided by solving the standard single sweep PNS model. As this initial condition is provided, the solution to the IPNS model is obtained by the ADE procedure, and the pressure is stored at all stations only

DOI: 10.1002/fld

in the subsonic region. Then, the process is repeated until the solution converges to a specified convergence criterion. To accelerate the convergence rate of the IPNS model, the underrelaxation procedure for pressure calculation in the subsonic region is applied as follows:

$$p_{k+1}=\Omega_p p_{k+1}+(1-\Omega_p)p_k, \quad \Omega_p<1 \tag{22}$$

where Ω_p denotes the pressure underrelaxation coefficient.

4. NUMERICAL RESULTS

The high-order accurate solution to hypersonic axisymmetric flows is obtained by implementing the fourth-order compact finite-difference method to the PNS and globally IPNS equations. First, the dispersive and dissipative properties of the compact method are studied. Then, the fourth-order compact method is implemented to the quasi-one-dimensional Euler equations to solve compressible flow inside the Shubin nozzle. Finally, the numerical solutions to the fourth-order compact PNS and IPNS schemes are presented for hypersonic flow over a blunt cone at Mach 8. A sensitivity study is performed to investigate the effects of grid size and numerical dissipation term on the accuracy of basic flow profiles and their derivatives. The present results are compared with those of other basic flow models to demonstrate the accuracy and efficiency of the proposed method.

4.1. Numerical stability analysis of compact schemes

To study the numerical stability of the compact schemes, the linear wave equation, $u_t+au_x=0$, which is a representative of the Navier–Stokes equations, is considered. Table I shows the stability bound of fourth-order central and third-order upwind compact schemes using different time discretization methods. Furthermore, the modified differential equations for the methods of this table were obtained; also the amplitude and phase errors of each of them were derived to study dispersive and dissipative properties of the methods. The study indicates that forward time-differencing is unconditionally unstable and backward time-differencing is unconditionally stable for the central compact scheme for the linear wave equation (see Table I). The stability bound

Table I. Stability bound of different space and time discretizations for the linear wave equation where $r=a\Delta t/\Delta x$ is the Courant number.

Space discretization	Time discretization	Stability bound
Central fourth-order compact	Forward	$r=0$
	Central	$r=0$
	Backward	$r\in\mathbb{R}$
Forward third-order compact	Forward	$r=0$
	Central	$r\in\mathbb{R}^-$
	Backward	$r\in\mathbb{R}-(0,\frac{1}{3})$
Backward third-order compact	Forward	$r=0$
	Central	$r\in\mathbb{R}^+$
	Backward	$r\in\mathbb{R}-(\frac{-1}{3},0)$

of the fourth-order compact scheme using backward time-differencing with the added sixth-order dissipation term is obtained in Appendix A.

4.2. *One-dimensional nozzle flow*

Since the Navier–Stokes equations have nonlinear terms that may lead to instability, before applying the compact method to the PNS equations, the fourth-order compact scheme is applied to the quasi-one-dimensional Euler equations for computing compressible flow inside the Shubin nozzle [8, 15] to gain some numerical experiences. The flow is supersonic along the nozzle. The flow conditions are fixed at the inlet and the characteristic boundary conditions are utilized at the outlet. A sixth-order dissipation term is used to stabilize the numerical instability of the scheme. Figure 2 shows the nondimensional pressure distribution along the nozzle using 20 grid points, whereas Table II gives the values of nondimensional pressure in the middle of the nozzle ($x=5$) and the corresponding error for different grid spacings. As shown in Figure 2, the value of numerical dissipation affects the results and less amount of dissipation is desired. The fourth-order accuracy of the method is demonstrated by comparison with the exact solution, as shown in Figure 3.

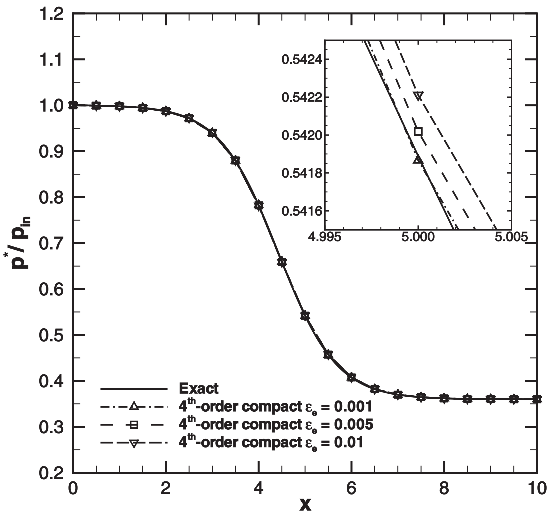

Figure 2. Comparison of computed and exact pressure distributions along the Shubin nozzle.

Table II. Comparison of computed and exact pressure values at middle of the nozzle ($x=5$) for $\varepsilon_e=0.001$.

Δx	Computed value	Error
1.0	0.5408528370900560	0.1036174769837750E−02
0.5	0.5418667374407204	0.2227441917335149E−04
0.25	0.5418886085873382	0.4032725555713768E−06
0.125	0.5418889858724278	0.2598746595694479E−07
Exact solution	0.5418890022432340	—

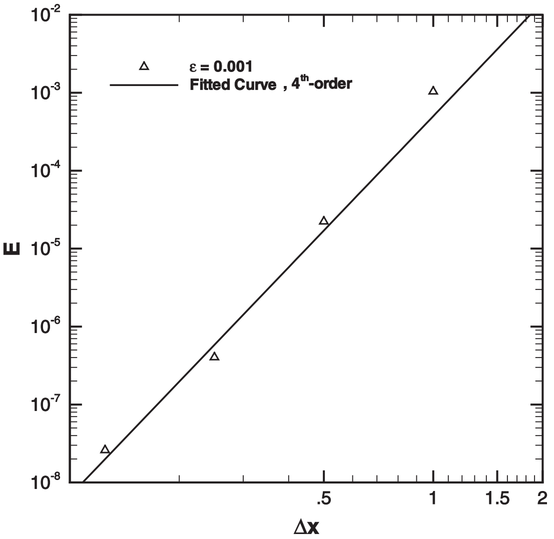

Figure 3. Order analysis of numerical solution of the Shubin nozzle by the fourth-order compact method.

4.3. *Hypersonic flow over a blunt cone*

The numerical solution to the PNS equations for computing supersonic/hypersonic flowfields is carried out by using the fourth-order compact finite-difference method. Both PNS and globally IPNS models are used. The geometry and the free-stream conditions are adapted to the wind-tunnel blunt cone experiment of Stetson *et al.* [16]. For this blunt cone, the flow conditions are a free-stream Mach number of $M_\infty = 8$, a free-stream unit Reynolds number of $Re_\infty/m = 8.2021\times 10^6$ and a free-stream temperature of $T^*_\infty = 54.3\,\text{K}$ (the starred variables are referred to the dimensional ones). The blunt cone has a half-angle of $\theta_\text{c} = 7^\circ$ and the study is performed at zero angle of attack. The blunt cone has a spherical nose radius of $R_\text{N} = 3.81\,\text{mm}$, and the free-stream Reynolds number based on this length is $Re_\infty = 31\,250$. For this case, a sensitivity study is performed for the basic state solution, including the profiles and their derivatives obtained from the high-order compact PNS and IPNS schemes, and the effects of grid size and numerical dissipation term used are discussed. All profiles and their derivatives calculated by the fourth-order compact PNS and IPNS models are presented at the marching station, $S^*/R_\text{N} = 175$.

The second-order central TLNS code [5, 13] is used to solve the flowfield in the nose region $S = S^*/R_\text{N} \leqslant 4.0$ with 80 grid points in the streamwise direction and 100, 200 and 400 grid points in the wall-normal direction to provide the initial data plane for the solution to the PNS and IPNS codes (see Figure 1). The marching stepsize for the PNS and IPNS codes, $\Delta\xi$, is chosen to be the same as that of the TLNS code, that is, $\Delta\xi = 0.05$. Figure 1 shows the regions solved by the TLNS and PNS equations. The figure also indicates the development of the velocity field computed by the PNS equations.

The present fourth-order compact PNS and IPNS codes have been thoroughly verified by comparison with those of the second-order PNS and IPNS codes [3, 4]. The details of these investigations can be found in References [6–8]. Herein, the present solutions based on the fourth-order compact PNS schemes are also compared with those of the TLNS and the Euler/second-order boundary-layer (EUBL) models. The TLNS model has been used by Esfahanian [5] and Herbert and Esfahanian [17] as a basic flow to study the stability analysis of hypersonic flow over the blunt cone at Mach 8 for the conditions of the experiment of Stetson *et al.* [16]. The numerical solution to the TLNS model was obtained by the Beam–Warming method [14] using a shock-fitting procedure. They devoted considerable effort to obtain an accurate solution to the TLNS model by employing the smallest possible numerical dissipation value. They emphasized the need for a correct calculation of the basic flow variables and also their derivatives as a prerequisite for flow stability computations. In the EUBL model, Stilla [18] used the second-order boundary-layer equations for investigating the flow stability analysis of the same case. The EUBL equations can be derived by an order-of-magnitude analysis of the Navier–Stokes equations or by the 'matched asymptotic expansion' approach. Note that the EUBL model is a multi-step solution and the IPNS solution [3, 4] is less cumbersome than the EUBL solution.

A grid independence study is conducted to evaluate the effects of grid size in the wall-normal direction on the flow variables. For this study, the Mach number profile is chosen due to its dependency on both momentum and energy equations. Figure 4 compares the Mach number profile computed by the second-order central and fourth-order compact PNS models at the desired station, $S^*/R_{\mathrm{N}} = 175$. The results of the second-order Beam and Warming method are performed for different grid points in the wall-normal direction. It is clear that $J_{\max} = 200$ is an adequate grid for the second-order method [3, 4]. It can be seen that the results of the fourth-order compact solution using $J_{\max} = 100$ are comparable with those of second-order solutions using $J_{\max} = 200$ and 400.

Figure 5 presents a comparison of the surface temperature distribution for the second-order central and fourth-order compact PNS models for different numbers of grid points in the wall-normal direction. The compact method with $J_{\max} = 100$ gives the same distribution as the second-order method with $J_{\max} = 400$. The effect of numerical dissipation order and value in the compact solution to the PNS model on the surface temperature using $J_{\max} = 100$ is examined in Figure 6.

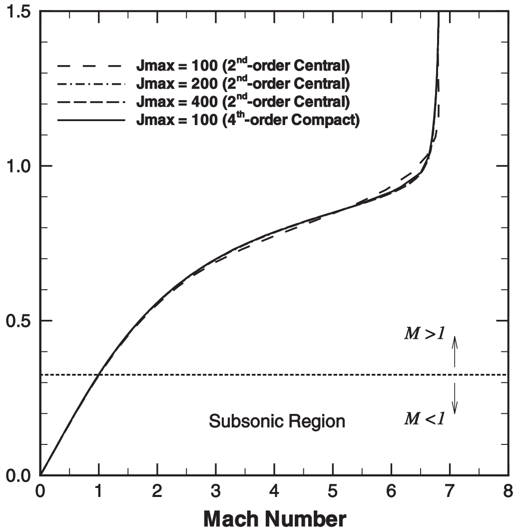

Figure 4. Comparison of Mach number profile for the second-order central and fourth-order compact PNS models for the blunt cone, $M_\infty = 8$ and $Re_\infty = 31\,250$ at $S = 175$.

DOI: 10.1002/fld

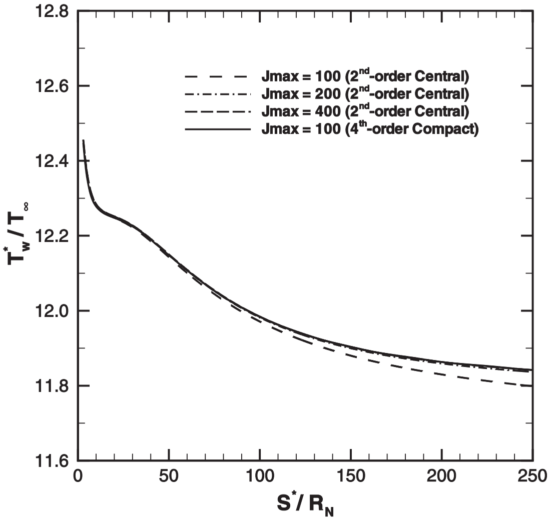

Figure 5. Comparison of surface temperature distribution for the second-order central and fourth-order compact PNS models for the blunt cone, $M_\infty = 8$ and $Re_\infty = 31\,250$.

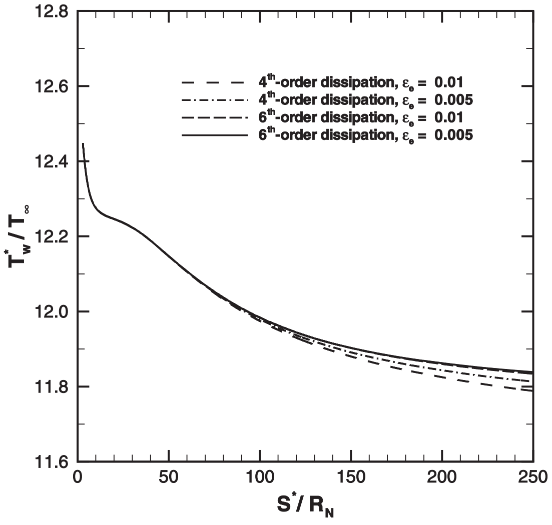

Figure 6. Effect of sixth-order and fourth-order dissipation terms on surface temperature distribution for the fourth-order compact PNS model for the blunt cone, $M_\infty = 8$ and $Re_\infty = 31\,250$.

No considerable difference is observed for the sixth-order dissipation, whereas the fourth-order dissipation significantly affects the surface temperature. The reason is that the numerical value of the sixth-order dissipation near the wall is much smaller than that of the fourth-order dissipation, with the same dissipation coefficient. The fourth-order dissipation term was also found to have significant effects on the surface temperature for the second-order method [3, 4]. A comparison of the skin friction coefficient for the second-order central and fourth-order compact PNS models for different number of grid points in the wall-normal direction is shown in Figure 7. It can be seen that the skin friction coefficient is less sensitive to the grid size than the surface temperature and the compact method provides more accurate results.

To verify the order of a numerical method in a specific problem, it is usual to compare the value of variables in the interior nodes among different grid sizes. However, in this simulation due to dependency of the shock position to the numerical solution and also due to nonuniformity of the grid, the position of the shock and consequently the position of the grid points in the wall-normal direction do not have the same location for different numbers of grid points. Because of this difficulty, one should select the surface variables for evaluating the accuracy of the method. However, the accuracy of the method is influenced by the boundary treatment used, which is a third-order compact finite-different scheme with respect to the first derivatives. For this study, the skin friction coefficient due to its dependency on the first derivative of the velocity is chosen to evaluate the numerical accuracy of the compact method. Three cases are considered for this analysis: $J_{\max}=100$, 200 and 400 where the finest grid is considered to be the exact solution. To avoid local effects, the following L_2-norm is defined:

$$e=\left(\int_{S_1}^{S_2} |\psi-\psi_{\text{exact}}|^2\,\mathrm{d}S\right)^{1/2} \quad \text{where } \psi=C_f \tag{23}$$

where S_1 is taken far enough to remove the effect of initial conditions. Using the above norm, the computed order of the compact method is obtained as

$$\log_2\left(\frac{e_{100}}{e_{200}}\right)=2.84 \text{ using } S_1=100,\ S_2=200$$

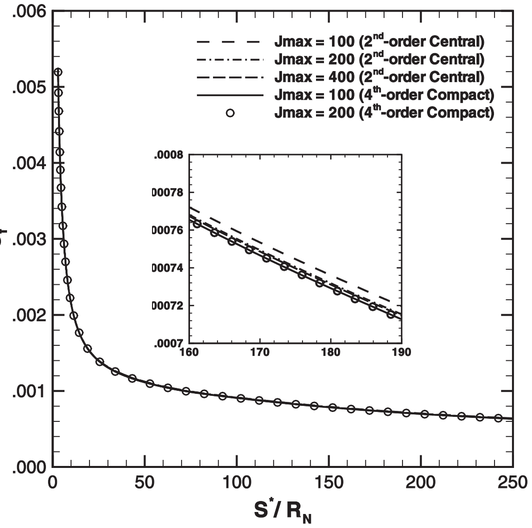

Figure 7. Comparison of skin friction coefficient distribution for the second-order central and fourth-order compact PNS models for the blunt cone, $M_\infty=8$ and $Re_\infty=31\,250$.

DOI: 10.1002/fld

which seems reasonable considering that the boundary treatment used is third order. However, the above value is observed to be dependent on S_1 and S_2 and the chosen variable and varies between 2.5 and 3.5.

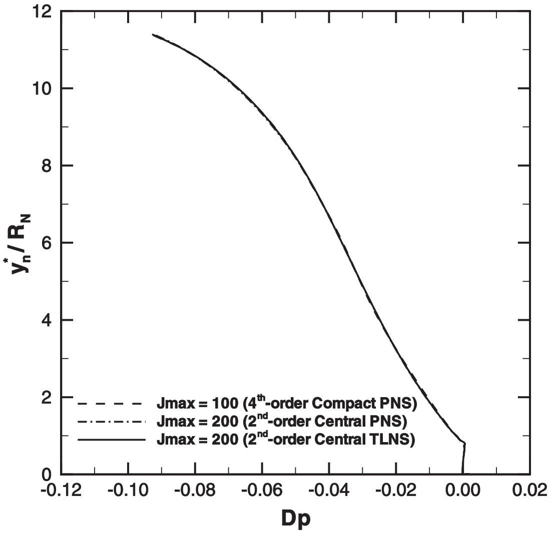

Figure 8. Comparison of first derivative of pressure profile for the second-order central and fourth-order compact PNS models and the TLNS model for the blunt cone, $M_\infty = 8$ and $Re_\infty = 31\,250$ at $S = 175$.

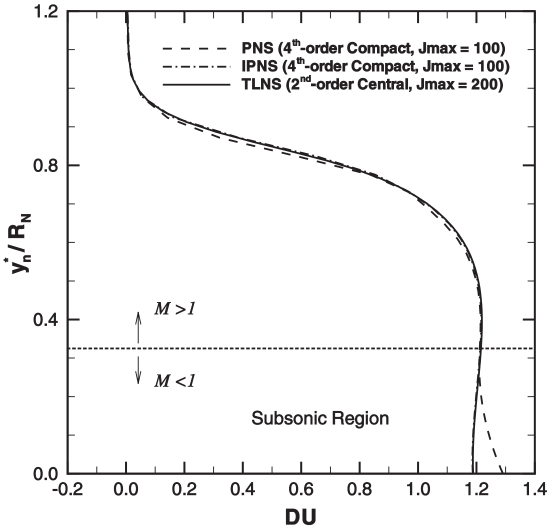

Figure 9. Comparison of first derivative of velocity profile for the fourth-order compact PNS and IPNS models and the TLNS model for the blunt cone, $M_\infty = 8$ and $Re_\infty = 31\,250$ at $S = 175$.

DOI: 10.1002/fld

Besides accurate computation of the basic flowfield, the accuracy of the first and second derivatives of the flow variables with respect to the wall-normal direction is crucial for the flow stability analysis of high-speed flows. In addition to the global accuracy, the main advantage of the present compact formulation for computing the flowfield is that the basic flow variables and their first and second derivatives are automatically calculated with the fourth-order accuracy and no intermediate computation of the derivatives, which usually produces oscillations in these profiles, is required. Hereinafter, the symbol D represents the derivative with respect to the wall-normal direction $y_n = y_n^*/R_N$. Figure 8 shows a comparison of the first derivative of the pressure profile Dp from the fourth-order compact PNS model using $J_{\max} = 100$ with that of the second-order PNS and TLNS models using $J_{\max} = 200$ at station 175 which shows no considerable difference among these curves. Note that the basic flow based on the TLNS model [5, 13] for the blunt cone studied herein is available for $J_{\max} = 200$ and $\bar{\beta} = 1.01$. Figure 9 shows a comparison of the first derivative of the streamwise velocity profile DU $(U = (u\xi_x + v\xi_y)/\sqrt{\xi_x^2 + \xi_y^2})$ from the fourth-order compact PNS and IPNS models using $J_{\max} = 100$ with that of the second-order TLNS model using $J_{\max} = 200$ at the desired station. The deviation of the PNS model is due to neglecting the explicit part of the streamwise pressure gradient in Equation (2), which is not omitted in the IPNS model; therefore, this deviation is completely compensated by the IPNS model. Although the results of the flowfield based on the IPNS and TLNS models are nearly the same, the IPNS model is computationally more efficient than the TLNS model. Thus, using the fourth-order compact IPNS scheme, a high-order accurate and efficient basic flow model can be provided. Figure 10 compares the first derivatives of the streamwise velocity profile DU from the IPNS model for the second-order central and fourth-order compact solutions. It is obvious that the results of the compact method with $J_{\max} = 100$ is comparable with those of the second-order method using $J_{\max} = 400$.

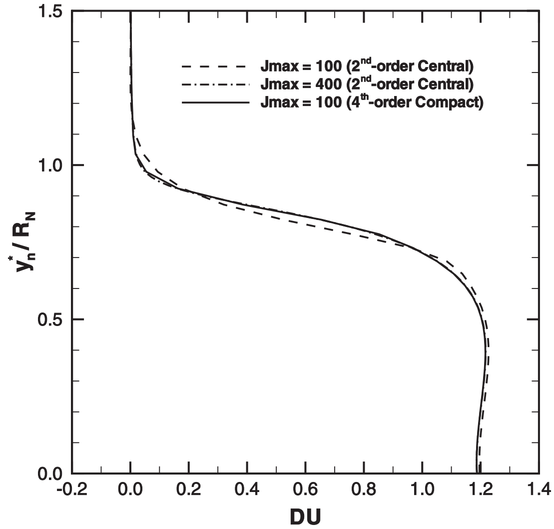

Figure 10. Comparison of first derivative of velocity profile for the second-order central and fourth-order compact IPNS models for the blunt cone, $M_\infty = 8$ and $Re_\infty = 31\,250$ at $S = 175$.

A sensitivity study is also performed for the higher derivatives of the flow variables. Figure 11 demonstrates the effect of grid refinement in the streamwise direction on the second derivative of the temperature profile D^2T computed by the fourth-order compact PNS model using $J_{\max}=200$ for different values of the marching stepsize $\Delta\xi$ at station 175. The figure shows that marching

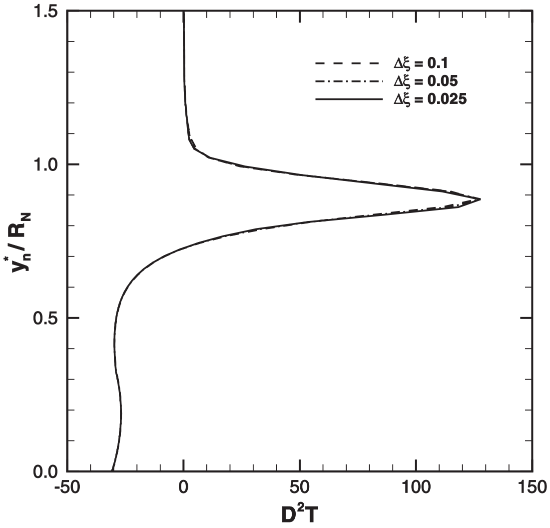

Figure 11. Effect of grid refinement in the streamwise direction for second derivative of temperature profile in the fourth-order compact PNS solution for the blunt cone, $M_\infty=8$ and $Re_\infty=31\,250$ at $S=175$.

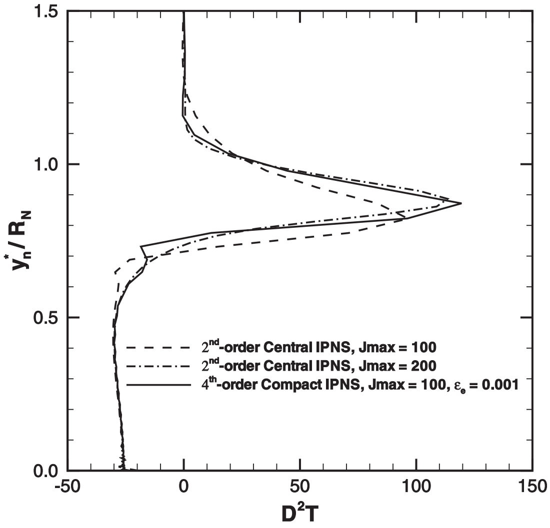

Figure 12. Comparison of second derivative of temperature profile for the second-order central and fourth-order compact IPNS models for the blunt cone, $M_\infty=8$ and $Re_\infty=31\,250$ at $S=175$.

DOI: 10.1002/fld

stepsize does not affect the D^2T profile. This is evident from the fact that the evolution of the flow in the streamwise direction at the afterbody region ($S \geqslant 74$) is very slow. To examine the improvement in the second derivatives of the flow variables, the profiles of D^2T for the second-order central and fourth-order compact IPNS models are shown in Figure 12. The results of $J_{\max} = 100$ for the compact method and those of $J_{\max} = 200$ for the second-order method are nearly the same except in an oscillation near $y_n \simeq 0.7$, which is close to high gradient region of the profile (the critical layer region). This oscillation is caused by the sixth-order dissipation term used. Figure 13 shows the values of the fourth element of dissipation vector, which correspond to the energy equation for different numbers of grid points and different values of dissipation coefficient. As expected, the amount of numerical dissipation decreases with increasing the number of grid points. As the grid becomes finer or a smaller dissipation value is used, the amount of dissipation becomes closer to zero. Figure 14 presents the effect of numerical dissipation on the second derivative of the temperature profile D^2T from the fourth-order compact IPNS model for different grids and different values of dissipation coefficient. It is clear that the oscillation in the second derivative of the temperature profile can be eliminated by using a finer grid, i.e. $J_{\max} = 140$, or by choosing a smaller amount of dissipation value, i.e. in the range of $\varepsilon_e = 0.0002$–0.0005 instead of 0.001. For fine grids, the value of ε_e can be in the range of 0.0001–0.001 without any considerable effect on the results; however, for smaller values of dissipation, very small wiggles may be seen near the wall region. Note that for the numerical dissipation values in the stability bound (see Appendix A), no obvious oscillations were seen in the results of the compact PNS schemes for the basic flow variables. It was found that in general for coarse grids, the dissipation term has a significant effect on the higher derivatives of the flow variables. Therefore, special attention should be paid in using the artificial dissipation for stabilizing the numerical instability of high-order compact finite-difference schemes to obtain accurate basic flow models.

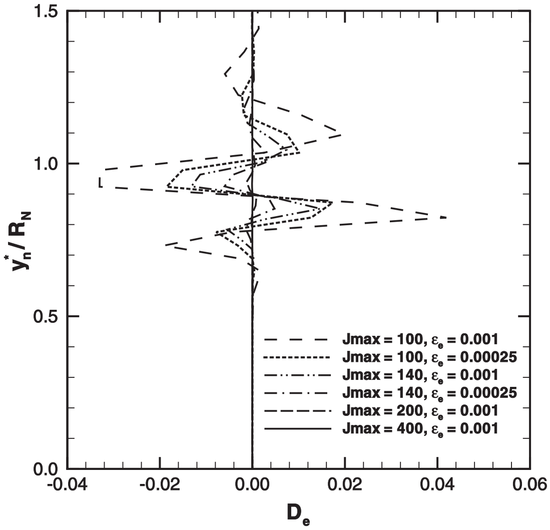

Figure 13. Distribution of sixth-order dissipation term for different numerical dissipations and grid spacings in the fourth-order compact PNS solution for the blunt cone, $M_\infty = 8$ and $Re_\infty = 31\,250$ at $S = 175$.

DOI: 10.1002/fld

To further analyze the difference between second-order central and fourth-order compact methods, which is independent of the numerical dissipation effect, the same profile, D^2T, is considered with different numbers of grid points as shown in Figure 15. It is found that the fourth-order compact method with $J_{\max}=140$ captures the maximum such as the second-order

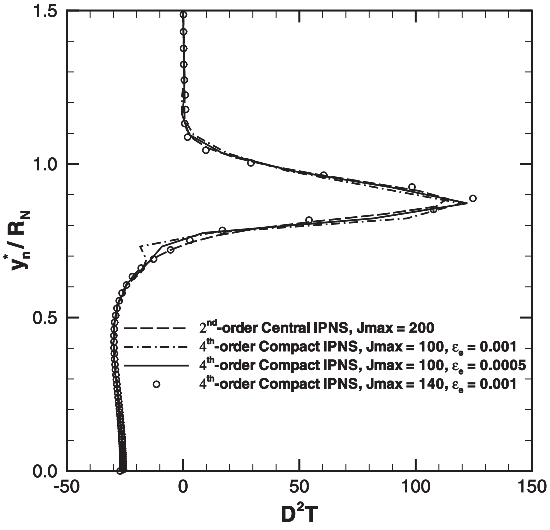

Figure 14. Effect of numerical dissipation value and grid size on second derivative of temperature profile in the fourth-order compact IPNS solution for the blunt cone, $M_\infty=8$ and $Re_\infty=31\,250$ at $S=175$.

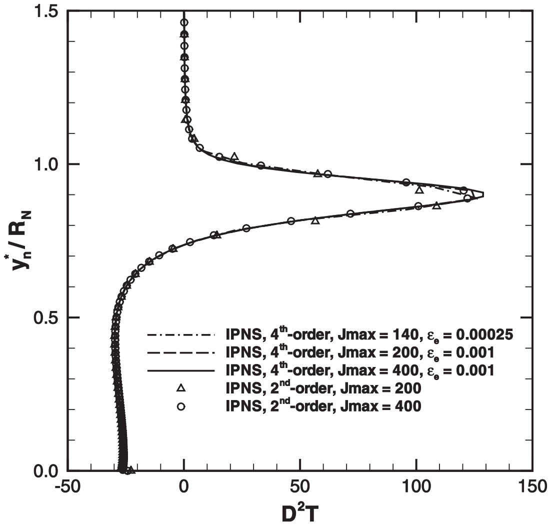

Figure 15. Comparison of second derivative of temperature profile for the second-order central and fourth-order compact IPNS models for different grid sizes for the blunt cone, $M_\infty=8$ and $Re_\infty=31\,250$ at $S=175$.

central with $J_{\max}=400$. As previously mentioned, by increasing the number of grid points, the effect of numerical dissipation becomes very less important (see Figures 13 and 14). Therefore, the difference between the results of the second-order central and fourth-order compact methods is due to the accuracy of the numerical methods used.

In Figure 16 the second derivative of the temperature profile D^2T is obtained by differencing the temperature values of the solution to the fourth-order compact IPNS model in two ways: second-order central differencing and fourth-order compact differencing. The figure shows that the maximum value of D^2T in the critical region is predicted better with compact differencing, especially for a lower number of grid points, i.e. $J_{\max}=100$. As the number of grid points increases, the accuracy of the higher derivatives of the basic flow profiles becomes independent of the way of computing the derivatives.

A comparison of the results obtained by using the proposed scheme with other methods is also performed. The present computations based on the fourth-order compact IPNS model are compared with those of the second-order IPNS model and also the TLNS and EUBL models. Figure 17 compares the temperature profiles computed by different basic flow models. The study shows that the results of these methods are in agreement with each other. The comparison of the second derivatives of the temperature profile in Figure 18 shows that the methods give nearly the same results. The results demonstrate that the compact method can capture the maximum of the second derivative of the profile near the critical layer more accurate than the other methods.

Finally, the CPU-time comparison of the various solutions for the same case is performed to show the efficiency of using the high-order compact PNS schemes. The present calculations using the PNS and IPNS schemes are performed on a 3.2-GHz Pentium IV computer. Figure 19 shows the convergence history of both second-order central and fourth-order compact IPNS models using $\Delta t/\Delta\xi=2.5$ and $\Omega_p=0.7$ for the blunt cone studied herein. These solutions are obtained with

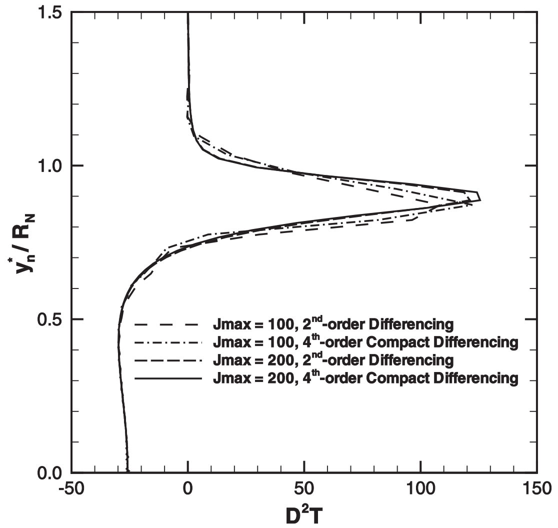

Figure 16. Comparison of second derivative of temperature profile for the second-order central and fourth-order compact differencing of the compact IPNS solution for the blunt cone, $M_\infty=8$ and $Re_\infty=31\,250$ at $S=175$.

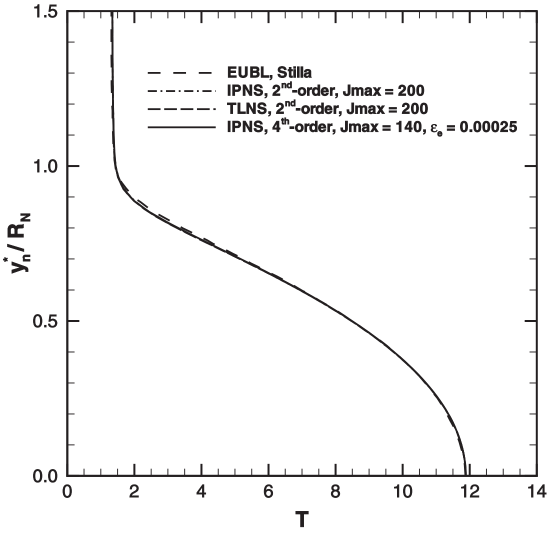

Figure 17. Comparison of temperature profile computed by different basic flows for the blunt cone, $M_\infty = 8$ and $Re_\infty = 31\,250$ at $S = 175$.

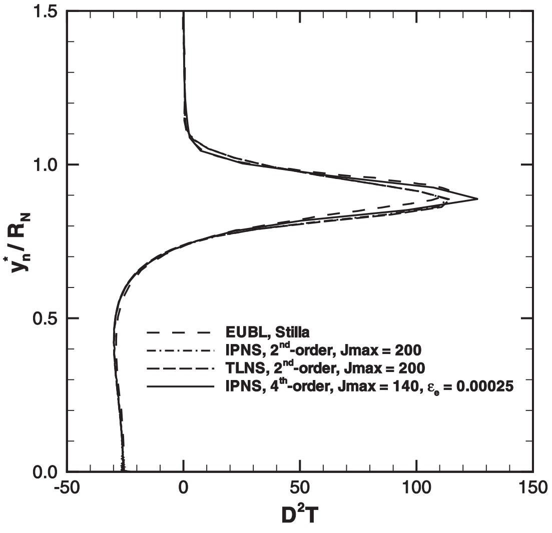

Figure 18. Comparison of second derivative of temperature profile computed by different basic flows for the blunt cone, $M_\infty = 8$ and $Re_\infty = 31\,250$ at $S = 175$.

$J_{\max} = 200$ for the global region $4 \leqslant S \leqslant 250$, which includes approximately 5000 marching steps ($\Delta\xi = 0.05$) for each global iteration. The computations are considered to be converged when the root mean square (RMS) of the relative change in pressure is less than 1×10^{-6}. The numbers of global iterations for convergence of the second-order central and fourth-order compact IPNS models are about 81 and 92, respectively. The computation times are about 9 and 105 min for

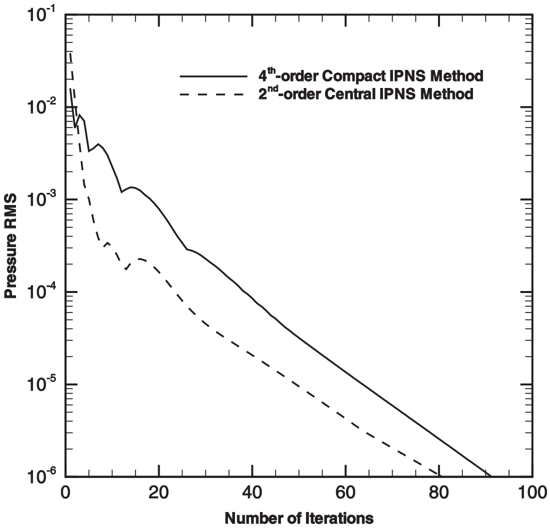

Figure 19. Convergence history of the second-order central and fourth-order compact IPNS models using $\Delta t/\Delta\xi = 2.5$ and $\Omega_p = 0.7$ for the blunt cone, $M_\infty = 8$ and $Re_\infty = 31\,250$.

the second-order central and fourth-order compact IPNS models (6 and 70 s for those of the PNS models), respectively. The CPU time of the second-order TLNS solution for the region $S \leqslant 250$ using (1300×200) grid points was about 260 h on a Cray Y-MP [5, 13]. It is clear that both fourth-order compact PNS and IPNS schemes are suitable for accurate and efficient computation of basic flow models in comparison with the TLNS scheme.

5. CONCLUSIONS

The numerical solution to the PNS schemes for computing supersonic/hypersonic axisymmetric flowfields is obtained by using the fourth-order compact finite-difference method. Both PNS and IPNS models are considered. Some significant conclusions regarding the present calculations based on the high-order compact PNS schemes are summarized as follows:

1. The present results indicate that surface variables are accurately computed by the compact method, whereas the second-order method shows considerable different results with different grid spacings. The compact method is capable of computing the flowfield variables, especially their derivatives, more accurately than the second-order method.
2. In addition to the global accuracy, the main benefit of using the present high-order compact formulation for the solution of the flowfield is that the derivatives of the flow variables, required for stability computations, are automatically calculated with the same accuracy of the flow variables and no intermediate computation of the derivatives, which usually produces oscillations in these profiles, is needed. Note that treating the Von Neumann boundary condition is much simpler with the compact method without loss of accuracy and tridiagonality.
3. It is demonstrated that the accuracy of the derivatives of the flowfield variables computed based on high-order compact methods is sensitive to the number of grid points, especially

the numerical dissipation. Using the compact method, no further clustering is needed near the wall and special attention should be paid on the critical layer. It is shown that by using high-order accurate methods, in addition to the basic flow variables, the accuracy of their derivatives can be improved; however, a suitable amount of numerical dissipation is crucial and improper choice of numerical dissipation may deteriorate the advantage of using high-order accurate methods. The study indicates that any practical development in high-order compact methods requires a more sophisticated numerical dissipation.

4. Although the results of the flowfield based on the IPNS, TLNS and EUBL models are almost identical, the IPNS model is computationally more efficient than the TLNS and EUBL models. Therefore, using the fourth-order compact IPNS model, a high-order accurate and efficient basic flow model can be provided.
5. The present study introduces the high-order compact solutions to the PNS schemes for providing accurate and efficient basic flow models to be used for the stability analysis and transition prediction of hypersonic axisymmetric flows.

APPENDIX A

Here, we study the stability of the fourth-order compact scheme for the linear advection–diffusion equation. Then, the convergence analysis of the numerical method is investigated. In [19], it was shown that the fourth-order compact method is unconditionally stable for the linear two-dimensional hyperbolic (wave) equation. In addition, in [20] an eigenspectrum analysis for the simple advection equation $u_t + au_x = 0$ for the second- and fourth-central and fourth-order compact schemes was performed and their stability discussed. Also, it was pointed out in [21] that the simple advection equation is a good model for the description and studying the properties of numerical approximations of hyperbolic systems. In the following, we use the Von Neumann stability analysis for the advection–diffusion equation, $u_t + au_x = \mu u_{xx}$.

Consider the one-dimensional linear advection–diffusion equation with the sixth-order dissipation term added to the right-hand side of the equation:

$$u_t + au_x = \mu u_{xx} + \varepsilon_e \frac{(\Delta x)^6}{(\Delta t)} u_{xxxxxx} \tag{A1}$$

Now using the compact differencing (Equation (10)) for the space discretization and the Euler implicit method for the time-marching scheme and also using the operator notation, we have

$$\begin{aligned}
u^{n+1} - u^n + rQ_x^{-1} D_x u^{n+1} &= bQ_{xx}^{-1} D_{xx} u^{n+1} + \varepsilon_e (\Delta\nabla)^3 u^n \\
r &= \frac{a\Delta t}{\Delta x}, \quad b = \frac{\mu \Delta t}{(\Delta x)^2} \\
Q_x u_i &= \frac{u_{i+1} + 4u_i + u_{i-1}}{6}, \quad D_x u_i = \frac{u_{i+1} - u_{i-1}}{2} \\
\Delta\nabla u_i &= u_{i+1} - 2u_i + u_{i-1} \\
Q_{xx} u_i &= \frac{u_{i+1} + 10u_i + u_{i-1}}{12}, \quad D_{xx} u_i = \Delta\nabla u_i = u_{i+1} - 2u_i + u_{i-1}
\end{aligned} \tag{A2}$$

Implementing the Von Neumann stability analysis, the amplification factor will be

$$
\begin{aligned}
&u_i^n = \sum \widehat{u}_i^n \mathrm{e}^{\mathrm{j} i k_m x}, \quad \mathrm{j}=\sqrt{-1}\\
&G = \frac{\widehat{u}_i^{n+1}}{\widehat{u}_i^n} = \frac{(\varepsilon_e(\Delta\nabla)^3+1)\mathrm{e}^{\mathrm{j} i k_m x}}{(1+rQ_x^{-1}D_x-bQ_{xx}^{-1}D_{xx})\mathrm{e}^{\mathrm{j} i k_m x}} = \frac{Q_xQ_{xx}(\varepsilon_e(\Delta\nabla)^3+1)\mathrm{e}^{\mathrm{j} i k_m x}}{(Q_xQ_{xx}+rQ_{xx}D_x-bQ_xD_{xx})\mathrm{e}^{\mathrm{j} i k_m x}}\\
&\quad = \frac{\dfrac{\cos\beta+5}{6}\dfrac{\cos\beta+2}{3}(\varepsilon_e(2\cos\beta-2)^3+1)}{\dfrac{\cos\beta+5}{6}\dfrac{\cos\beta+2}{3}-b\dfrac{\cos\beta+2}{3}(2\cos\beta-2)+\mathrm{j}(r\sin\beta)\dfrac{\cos\beta+5}{6}}\\
&\quad = \frac{(\cos\beta+5)(\cos\beta+2)(\varepsilon_e(2\cos\beta-2)^3+1)}{(\cos\beta+5)(\cos\beta+2)-6b(\cos\beta+2)(2\cos\beta-2)+\mathrm{j}3(r\sin\beta)(\cos\beta+5)}\\
&0<\beta=k_m\Delta x<\pi
\end{aligned}
\tag{A3}
$$

For stability, we require $|G|\leqslant 1$. Since r is appeared in the imaginary part of the denominator, increasing r decreases $|G|$. Consequently, if $|G|\leqslant 1$ for $r=0$, then $|G|\leqslant 1$ for all $r\in\mathbb{R}$. In the other words, stability for $r=0$ is sufficient for stability of all $r\in\mathbb{R}$. Considering the above statement, we analyze the stability condition for $r=0$. Hence,

$$G(\beta)=\frac{(\cos\beta+5)(\varepsilon_e(2\cos\beta-2)^3+1)}{(\cos\beta+5)-6b(2\cos\beta-2)}=\frac{(\cos\beta+5)(1-8\varepsilon_e(1-\cos\beta)^3)}{(\cos\beta+5)+12b(1-\cos\beta)} \tag{A4}$$

Since $b\geqslant 0$ and $1-\cos\beta\geqslant 0$, the denominator is a positive number and increases with increasing b. Therefore, $|G|$ decreases with increasing b, which shows that the stability of the inviscid equation implies the stability of the viscous equation. By eliminating the viscous term, we have

$$
\begin{aligned}
&G(\beta)=1-8\varepsilon_e(1-\cos\beta)^3\\
&|G(\beta)|\leqslant 1 \Rightarrow |1-8\varepsilon_e(1-\cos\beta)^3|\leqslant 1 \Rightarrow 0\leqslant\varepsilon_e(1-\cos\beta)^3\leqslant\tfrac{1}{4}
\end{aligned}
\tag{A5}
$$

Since $1-\cos\beta\geqslant 0$ and its maximum occurs at $\beta=\pi$, then

$$0\leqslant 8\varepsilon_e\leqslant\tfrac{1}{4}\Rightarrow 0\leqslant\varepsilon_e\leqslant\tfrac{1}{32} \tag{A6}$$

This bound for ε_e is a sufficient condition for the stability for all $b\geqslant 0$, $r\in\mathbb{R}$ and $0\leqslant\beta\leqslant\pi$. However, for the inviscid case ($\mu=b=0$) from Equation (A2) we have

$$
\begin{aligned}
&G(\pi)=1-64\varepsilon_e\\
&|G(\pi)|\leqslant 1\Rightarrow 0\leqslant\varepsilon_e\leqslant\tfrac{1}{32}
\end{aligned}
\tag{A7}
$$

which shows that this bound is also necessary for the inviscid case for all $r\in\mathbb{R}$. Figure A1 shows the absolute value of amplification factor G for the inviscid case for different values of dissipation coefficient ε_e. Preparing the same test for the viscous equation (A3), we have

$$
\begin{aligned}
&G(\pi)=\frac{(-1+5)(-1+2)(\varepsilon_e(-2-2)^3+1)}{(-1+5)(-1+2)-6b(-1+2)(-2-2)}=\frac{(\varepsilon_e(-4)^3+1)}{1+6b}\\
&|G(\pi)|\leqslant 1\Rightarrow\left|\frac{(\varepsilon_e(-4)^3+1)}{1+6b}\right|\leqslant 1\Rightarrow -\frac{3b}{32}\leqslant\varepsilon_e\leqslant\frac{1+3b}{32}
\end{aligned}
\tag{A8}
$$

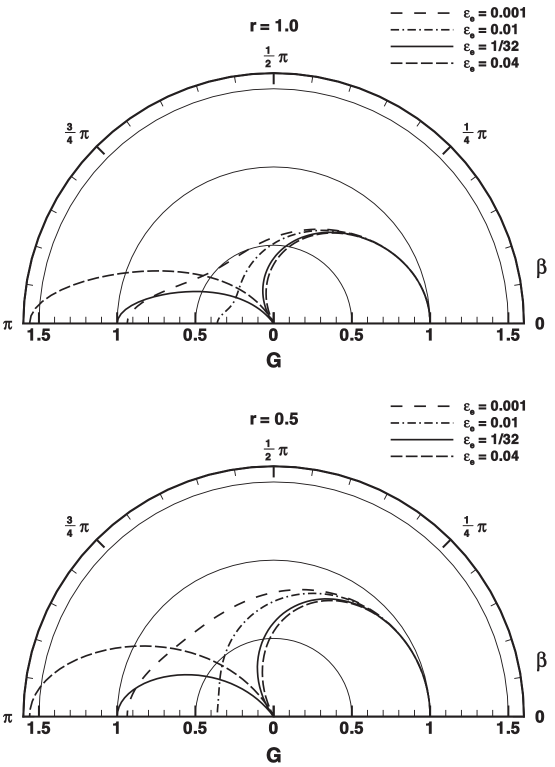

Figure A1. Amplification diagram (G) of the fourth-order compact method with the sixth-order dissipation term for the one-dimensional wave equation ($r = a\Delta t/\Delta x = 0.5, 1.0$).

which gives the necessary condition for the viscous case for all $r \in \mathbb{R}$. Again, the stability bound for the linear advection equation can be obtained by setting $\mu = b = 0$

$$0 \leqslant \varepsilon_e \leqslant \tfrac{1}{32} \tag{A9}$$

The convergence of the numerical solution may be shown using the Lax equivalence theorem [9, 22]. The modified differential equation of the Euler implicit integration of the fourth-order compact method for the linear advection equation, $u_t + au_x = 0$, is as follows:

$$\begin{aligned} u_t + au_x = {} & \frac{a^2\Delta t}{2}u_{xx} - \frac{a^3(\Delta t)^2}{3}u_{xxx} + \frac{a^4(\Delta t)^3}{4}u_{xxxx} \\ & - \frac{a[36a^4(\Delta t)^4 - (\Delta x)^4]}{180}u_{xxxxx} + O[(\Delta x)^m(\Delta t)^{5-m}], \quad m = 0, 2, 4 \end{aligned} \tag{A10}$$

It can be seen that the method is consistent with the original equation as the grid is refined. According to the Lax equivalence theorem, the numerical solution is convergent to the exact solution in the stability bound (Equation (A9)) of the proposed scheme.

ACKNOWLEDGEMENTS

The authors would like to thank the University of Tehran and Sharif University of Technology for financial support of this project. The authors would also like to thank assistant professor Sarmad Ghader for his valuable comments on the compact schemes.

REFERENCES

1. Tolstykh AL. *High Accuracy Non-centered Compact Difference Schemes for Fluid Dynamics Applications*. World Scientific: Singapore, 1994.
2. Lele SK, Tatineni M. Compact finite different schemes with spectral-like resolution. *Journal of Computational Physics* 1992; **103**:16–42.
3. Esfahanian V, Hejranfar K. Accuracy of parabolized Navier–Stokes schemes for stability analysis of hypersonic axisymmetric flows. *AIAA Journal* 2002; **40**(7):1311–1322.
4. Hejranfar K. Computation and stability analysis of hypersonic axisymmetric flows using parabolized schemes. *Ph.D. Thesis*, University of Tehran, March 2002.
5. Esfahanian V. Computation and stability analysis of laminar flow over a blunted cone in hypersonic flow. *Ph.D. Thesis*, Ohio State University, Columbus, June 1991.
6. Esfahanian V, Hejranfar K, Darian HM. Implementation of compact finite-difference method to parabolized Navier–Stokes equations. *The 13th Annual Conference of the Computational Fluid Dynamics Society of Canada*, *CFD 2005*, Newfoundland, Canada, 2005.
7. Esfahanian V, Hejranfar K, Darian HM. Implementation of compact finite-difference method to iterative parabolized Navier–Stokes equations. *The 25th Congress of International Council of the Aeronautical Sciences* (*ICAS*), Hamburg, Germany, 2006.
8. Darian HM. Computation of parabolized Navier–Stokes equations using compact finite-difference method. *MS Thesis*, University of Tehran, September 2004.
9. Tannehill JC, Anderson DA, Pletcher RH. *Computational Fluid Mechanics and Heat Transfer* (2nd edn). Taylor and Francis: Washington, DC, 1997.
10. Vigneron YC, Rakich JV, Tannehill JC. Calculation of supersonic viscous flow over delta wings with sharp subsonic leading edges. *AIAA Paper 78-1137*, July 1978.
11. Schiff LB, Steger JL. Numerical simulation of steady supersonic viscous flow. *AIAA Journal* 1980; **18**(12): 1421–1430.
12. Barnett M, Davis RT. Calculation of supersonic flows with strong viscous–inviscid interaction. *AIAA Journal* 1986; **24**(12):1949–1955.
13. Esfahanian V, Herbert Th, Burggraf OR. Computation of laminar flow over a long slender axisymmetric blunted cone in hypersonic flow. *AIAA Paper 92-0756*, January 1992.
14. Beam RM, Warming RF. An implicit factored scheme for the compressible Navier–Stokes equations. *AIAA Journal* 1978; **16**(4):393–402.
15. Shubin CR, Stephens AB, Glaz HM, Donaldson. Steady shock tracking and Newton's method applied to one-dimensional duct flow. *Journal of Computational Physics* 1981; 364–374.
16. Stetson KF, Thompson ER, Donaldson JC, Siler LG. Laminar boundary layer stability experiments on a cone at Mach 8. Part 2: blunt cone. *AIAA Paper 84-0006*, January 1984.
17. Herbert T, Esfahanian V. Stability of hypersonic flow over a blunt body. *CP-514*, *AGARD*, May 1992.
18. Stilla J. Engineering transition prediction for a hypersonic axisymmetric boundary layer. *Journal of Aircraft* 1994; **31**(6):1358–1364.
19. Ekaterinaris JA. Implicit, high-resolution, compact schemes for gas dynamics and aeroacoustics. *Journal of Computational Physics* 1991; **156**:272–299.
20. Ekaterinaris JA. Implicit high-order-accurate-in-space algorithms for the Navier–Stokes equations. *AIAA Journal* 2000; **38**(9):1594–1602.
21. Vichnevetsky R, Bowles JB. *Fourier Analysis of Numerical Approximations of Hyperbolic Equations*. SIAM Series in Applied Mathematics. SIAM: Philadelphia, PA, 1982; 19–34.
22. Leveque RJ. *Finite-volume Methods for Hyperbolic Problems*. Cambridge Texts in Applied Mathematics, 2004.

DOI: 10.1002/fld